Nested Dual-chamber Origami (NDO) Actuator with Pressure Compounding and Enhanced Payload

Xiaohuang Liu[1][0009-0002-8815-695X], Zhonggui Fang[1][0000-0003-4988-4233], Shaowu Tang[1][0009-0007-7563-6862], Fang Chen[1][0009-0005-2913-260X], Sicong Liu[1,2(✉)][0000-0002-1872-5283], Hongqiang Wang[1][0000-0002-7286-7514], Zheng Wang[1][0000-0002-7726-0770], Jian S Dai[1(✉)][0000-0002-9729-1662]

[1] Department of Mechanical and Energy Engineering, Southern University of Science and Technology, Shenzhen 518000, China

[2] Guangdong Provincial Key Laboratory of Intelligent Morphing Mechanisms and Adaptive Robotics, Harbin Institute of Technology (Shenzhen), Shenzhen, China 518055

liusc@sustech.edu.cn

daijs@sustech.edu.cn

Abstract. Soft robots hold interaction compliance and safety over rigid-body robots for promising adaptation and unique motion modes in unstructured environments, but weak payload due to the inherent compliance limits the task execution. Enhancing the payload for the classic pneumatic soft actuator remains a challenge, with the physical limitation of negative pressure supply less than 1 atm and buckling of thin-walled body. Previous works focused more on single-chamber structural promotion, such as stacking, directional constraint, and novel configuration design, while they could not completely avoid the abovementioned physical limitation. In this work, we proposed the nested dual-chamber origami actuator by integrating the Yoshimura origami with pleated origami to generate bidirectional motion via compounding of positive and negative pressure actuation within different chambers. Through the all-time intervention of the positive pressure, the proposed actuator enables enhancing bidirectional payload, especially in contraction. The design and fabrication are analyzed to prototype, and the statics models are derived to reveal the relationship between the pressure compounding and output force with the experimental validation. The experimental results show that the nested actuator can initially improve by 12.5% payload by the structural assembly while achieving even 162% payload enhancement in the contraction process through dual-chamber pneumatic compounding, compared to the common single-chamber Yoshimura actuator without diminishing the payload performance in the elongation direction at the same time. This nested design offers a novel approach to enhancing payload of soft actuators and has the potential to be further expanded into other motion forms.

Keywords: Nested dual-chamber origami, Pneumatic actuator, Payload enhance.

1 Introduction

Due to the advantage of being compliant, continuum, and customizable, soft robots have attracted rising attention in fields, such as bionics [1-6], healthcare [7-8] and industrial application [9]. As a crucial part of soft robots, soft actuators have been widely studied in actuation forms and the induced variety motion

capabilities. Through the actuation methods of fluid [10-11], electricity [12-13], and shape memory alloys [14-15], soft actuators exhibit versatile motion forms such as bending [16], twisting [17], rotation [18] as well as multi-direction [19]. Among them, the bidirectional linear actuator implemented by pneumatic actuation is one of the most applied due to simplicity, portability, and large actuation deformation [10]. However, their payload greatly limits the potential applications of pneumatic actuators.

Many researches have been conducted to improve the payload performance of soft pneumatic actuators: (1) Increasing the cross-sectional area of the actuator or combining multiple actuators in parallel are the most direct methods that can multiply the output force [20-21], while this method inevitably results in multiplying the overall size. (2) The actuation-direction output force can be enhanced by employing additional constraints, using fiber wrapping on the actuator's side with a staggered helical path [16,22] show significant enhancement in improving the axial deformation and payload capacity for silicone-based soft actuators. (3) Rigid-flexible coupling has been developed [23-25], showing an effective and promising mechanical performance by strategically placed constraints to regulate compliance. However, the rigid-component introduction inevitably reduces the dimension of the actuator's adaptability. (4) Folding-based structures have brought about more possibilities for soft actuators to further develop versatile designs and enhance payload capacity in recent years [26-28].

These various methods to enhance the payload of soft actuator have effectively expanded the application fields. However, enabling high bidirectional payload to satisfy wider operational requirements is still a significant challenge for pneumatic soft actuators. This is primarily due to the physical limitation of negative pressure, which is inherently restricted to below 1 atm, far lower than positive pressure. When the actuator performs bidirectional motions pneumatically, it is common for the positive and negative pressures to produce opposite motions, respectively. The payload limitation always exists in the negative-pressure movement, especially when the negative-pressure supply needs to be further limited to avoid the common issue of buckling in the thin-walled structure of soft actuators [29].

In this work, we propose the Nested Dual-chamber Origami (NDO) structure together with the Compounding of Positive and Negative Pressure Actuation (CPNPA) method to tackle the above-mentioned issues in classical single-chamber soft actuators. Distinctive from conventional pneumatic soft actuators with great elongation-process payload but weak inversion, we coaxially nest an origami structure that performs contraction during positive pressure inside another origami structure that performs elongation during positive pressure. The proposed NDO actuator enables both bidirectional-motion payloads to be executed and enhanced by positive pressure, thereby presenting a large bidirectional payload performance. Based on this mechanism, a 3D-printed compact nested soft actuator prototype was designed, consisting of a Yoshimura Origami (YO) structure outside and Pleated Origami (PO) structure inside, and was capable of enhancing payload without sacrificing the supplied pressure range. The main contributions are as follows:

(1) The concept of NDO structure together with CPNPA method, incorporating the positive pressure with the negative pressure in both actuation directions to enhance the bidirectional payloads for the pneumatic soft actuators.

(2) For analysis and experimental validation, a compact NDO actuator prototype was designed and fabricated based on the proposed NDO structure, generating doubled payload capacity without buckling within the same negative-pressure limitation.

This paper is organized as follows: The concept of NDO structure is introduced in Section 2, followed by the mechanical design and fabrication of NDO actuator in Section 3. Section 4 presents the statics modeling of the NDO actuator, with experimental validation in Section 5. The conclusion and future

work are drawn in Section 6.
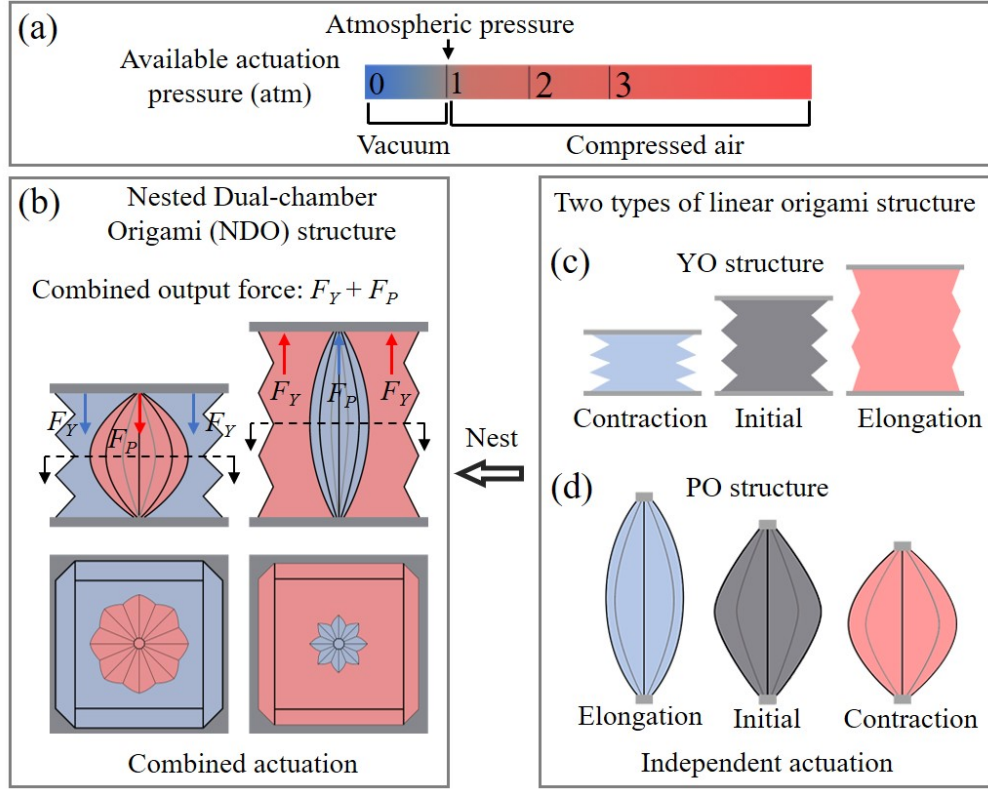
2   Concept of NDO Structure

Fig. 1. The concept of NDO structure. (a) The maximum negative differential pressure is 1atm, much lower than the positive pressure, which limits the force performance in the direction driven by negative pressure. (b) The overview of the proposed structure. The NDO structure consists of two origami chambers, by nesting the chambers coaxially, the strategy of dual-chamber compounding driving is realized. With the inner chamber under positive pressure and the outer chamber under negative pressure, the NDO structure presents a contraction movement and force. When converting the pressure state of both chambers, the NDO structure presents an elongation movement and force. Among them, (c) The YO structure produces axial elongation when pressurized and axial contraction when depressurized, (d) The PO structure produces axial contraction when pressurized and axial elongation when depressurized.

The core spirit of the proposed NDO structure is to coaxially integrate two different origami structures that perform opposite direction motion during positive and negative pressure, and nests them together to generate bidirectional motion and payload through the CPNPA in different chambers. Unlike the existing methodologies that seldom explored the bidirectional simultaneous payload enhancement with the physical suppling limitation of the negative pressure (Fig. 1a) on one side, due to the CPNPA method, the negative-pressure alone case is avoided, and the bidirectional payload can be well improved.

Here, a common YO structure (Fig. 1c) with linear actuation motion was chosen as the outer chamber structure, which performed elongation during positive pressure and contraction under negative pressure. As the inner chamber structure needs to perform opposite directional motion within the same pressure, the PO structure (Fig. 1d) was selected, with only little impact on the cross-sectional area of the outer

chamber when nested, making it possible to decouple the analysis of two structures. Since both the stroke and contractive force of the PO structure when inflated will significantly reduce with the increasement of the end face area, the PO structure is set to be the inner chamber in order to possess relatively small end face area. By coaxially nesting of the aforementioned parts, the NDO structure was constructed (Fig. 1b) while retaining the motion capability in both directions of each single-chamber origami structure. When performing contraction motion, to avoid structural buckling, the YO chamber driven by limited negative pressure exerted a diminutive force while the PO structure chamber driven by nearly unlimited positive pressure could significantly enhance the output force in the same direction. Besides, even though the elongation process showed great payload capability when the YO chamber was supplied with positive pressure, the PO structure chamber could also provide enhancement.

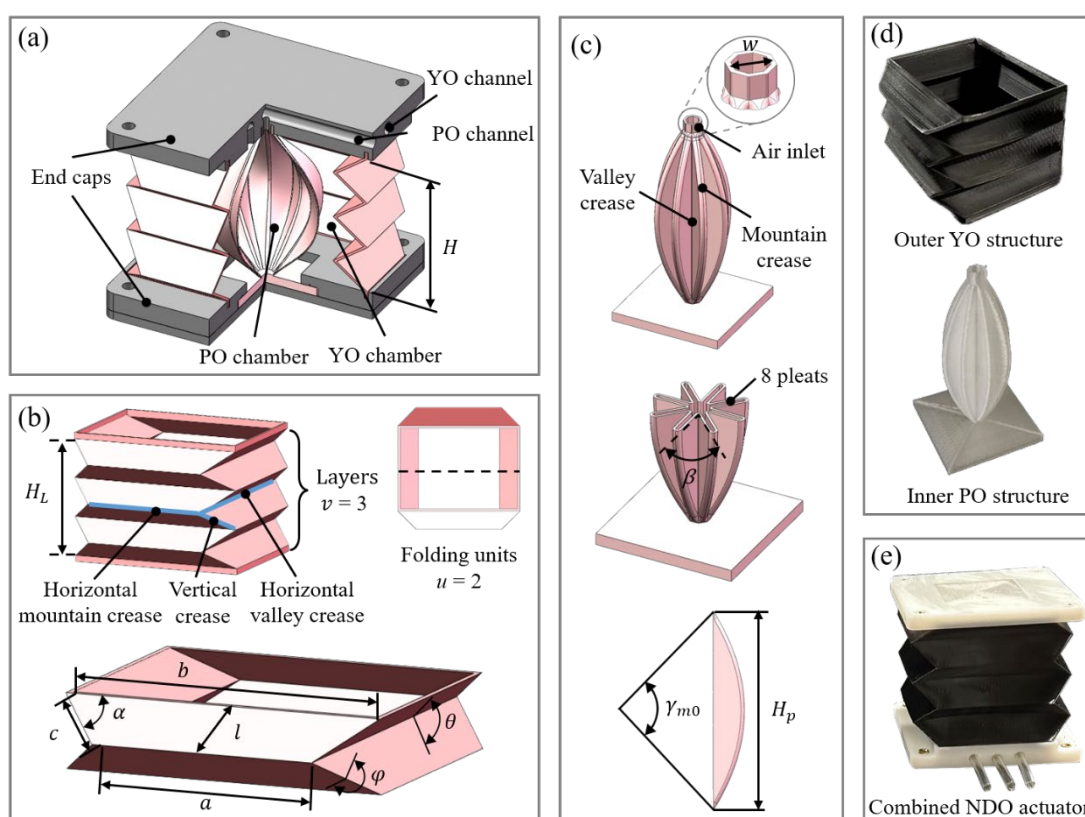# 3   Design and Fabrication of NDO Actuator

Fig. 2. Design of NDO actuator. (a) The main components of the overall assembly include three end caps that integrate air inlets and channels of dual chambers. (b) YO structure consists of 3 identical folding layers, and each layer includes two same folding units. (c) PO structure with eight same pleats. (d) Both the actuators were fabricated in TPU by FDM. (e) End caps fabricated in photosensitive resin by SLA, connect the actuators at both ends to form the NDO actuator.

A pneumatic actuator design is proposed to nest the two selected origami structures and ensure absolute tightness, consisting of both origami structures and three end caps which are embedded with corresponding air channels and connection bits for fixing (Fig. 2a). To facilitate 3D-printed fabrication, the PO structure was designed in the maximum-length state initially with a bottom-end air inlet (Fig. 2c). Eight identical pleats were evenly distributed around the circumference, with the angle between adjacent

pleats $\beta = \pi/4$. The mountain crease of the pleats was an arc, and valley crease was straight. As for the YO structure (Fig. 2b), we selected a quadrilateral cross-section, the most simplified side number, with three identical unit layers.

It is assumed that the mountain creases of PO structure keep the shape of an arc without change in the length during the deforming process and match the maximum value when they become semicircle arc. Meanwhile, the YO structure exhibits an almost constant radial size inside, during deformation. Both selected structures have been documented to be designed in various-size prototypes [4,20,30], making it possible to obtain the large axial motion range and avoid structural interference. To avoid radial contact, particularly during the contraction process, the following geometric conditions should be matched:

$$\frac{w}{2} + \frac{\gamma_{m0}H_P}{\pi \sin\left(\frac{\gamma_{m0}}{2}\right)} \leq a \tag{1}$$

$$H_P \leq 6l_0 \tag{2}$$

Where w is the width of the octagonal air inlet, H_P is the height of PO structure, a is the mountain horizontal crease of YO structure, γ_{m0} is the angle of the mountain-crease arc in the initial state, l_0 is the Height of trapezoid facets.

Table1. Geometry parameters of the proposed NDO actuator

Symbol	Parameter	Value
E	Young's modulus	30MPa (TPU 95A)
t	Thickness of YO structure	0.75mm
H_{Y0}	Height of YO structure	48mm
u	Folding units in one layer	2
v	Folding layers	3
a, b, c	Edges of trapezoid facet	50mm, 71.62mm, 7.26mm
l_0	Height of trapezoid facets	13.45mm
α	Angle of trapezoid	51.21°
θ_0	Dihedral angle at horizontal crease	73°
φ_0	Dihedral angles at vertical crease	310.25°
t_P	Thickness of PO structure	0.6mm
H_{P0}	Height of PO structure	60mm
γ_{m0}	Angle of the mountain-crease arc	70°
w	width of the octagonal air inlet	5.31mm
H	Height of NDO actuator	55mm

The detailed geometry parameters of the proposed nested actuator with two kinds of origami are listed in Table 1. As shown in Fig. 2d, through 3D-printed method of FDM (Fused Deposition Modeling) (Raise 3D Inc., Pro2), both origami structures were easily and quickly fabricated by TPU (eSUN Inc., 95A) with wall thickness of 0.75mm (YO structure) and 0.6mm (PO structure), which reduced the overall stiffness after ensuring significant tightness to benefit pneumatic actuation. In order to ensure the airtightness of the origami structure during the FDM printing process, we set the overlap of the printing path to 50% and adjusted the layer height to 0.12mm. This ensures the density of the same layer and the tightness of the interlayer connection. We also reduced the printing speed to 25mm/s to prevent the printing nozzle from affecting the positional stability of the thin-walled soft cavities when moving rapidly. The end caps (photosensitive resin) were fabricated by SLA (Stereo Lithography Appearance) and bonded with the origami structures by glue for overall tightness, air-supply smoothness, and structure compactness. The end caps have deep connection slots to link with the origami components, improving the shear-force bearing performance of NDO actuator. All components were assembled to construct the NDO actuator

prototype as shown in Fig. 2e. The origami structures were initially preloaded and antagonistic with each other.

4   Modeling of NDO Actuator

The concept of enhancing the bidirectional payload of soft actuators by NDO structure is based on the CPNPA method. It is essential to obtain a statics model to reveal their interconnections, as a guide for performance analysis and pneumatic actuation. As mentioned above, based on the static equilibrium, the output force of NDO actuator consists of two independent parts,

$$F = F_{YO} + F_{PO} = F_{YOH}(H_Y) + F_{YOP}(P_Y) + F_{POH}(H_P) + F_{POP}(P_P) \tag{3}$$

Where F is the output force of NDO actuator, F_{YO}, and F_{PO} are the output force of YO chamber and PO chamber respectively. Both F_{YO} and F_{PO} are generated from two kinds of force: (1) the forces generated by the stiffness of the chambers, F_{YOH} and F_{POH}, working as the resisting force, which are related to the height of the chambers, H_Y and H_P (subscript Y represents YO chamber, P represents PO chamber) (2) the forces generated by the pressure difference, F_{YOP} and F_{POP}, working as the driving force for the motion process, which are related to the pressure difference, P_Y and P_P. To elucidate the statics model of YO chamber, F_{YOSH} and F_{YOSP} are analyzed separately.
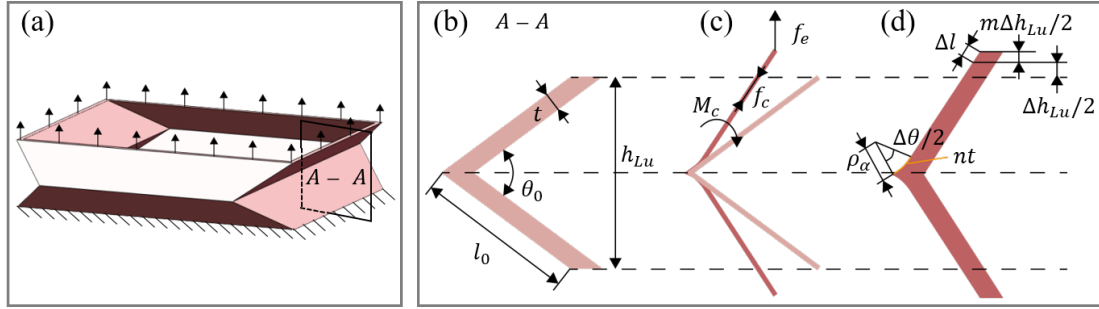

Fig. 3. The analysis of the resisting force of YO chamber based on the small-strain folding (SSF) principle. (a) Single layer of the YO structure subjected to external force. (b) Schematic representation of the crease in initial state. (c) when subjected to external force f_e, the corresponding bending moments M_c and resistance forces f_c are generated. (d) The structural illustration of the small-strain folding (SSF) principle.

As the force generated by self-deformation of YO chamber, F_{YOH} can be derived by the small-strain folding (SSF) principle [29]. The SSF principle attributes the macroscopic resistance of the actuator primarily to the bending moment induced by the structural flexure at the crease and the in-plane tension resulting from in-plane stretching (Fig. 3c). By using the principle of virtual work, when YO chamber is subjected to axial force (Fig. 3a), the following relationship is established as,

$$F_e \cdot dH_Y = \Sigma M_\theta \cdot d\theta + \Sigma M_\varphi \cdot d\varphi + \Sigma f_\theta \cdot dl_\theta \tag{4}$$

Where M_θ and θ are the out-of-plane bending moment and angular displacement around the horizontal creases, respectively, M_φ and φ are the out-of-plane bending moment and angular displacement around the vertical creases, respectively. f_θ and l_θ are the in-plane stretching force and displacement of the facets, respectively. F_{YOSH} and F_e are equal in magnitude but opposite in direction.

By converting the three-dimensional crease into a two-dimensional rod structure (Fig. 3b), the range of the bending region and the in-plane tension extent of the actuator are determined by nt and $m\Delta h_{Lu}/2$ (Fig. 3d). According to SSF principle, by incorporating the statics analysis of combined tension or compression, and bending deformations from material mechanics, the relationship between F_{YOH} and H_Y

can be further derived as follows,

$$F_{YOH} = F_e = \frac{uv(a+b)Et^2}{6n(H_Y - H_{Y0})}\left(\arcsin\left(\frac{H_Y}{2vl_0}\right) - \arcsin\left(\frac{H_{Y0}}{2vl_0}\right)\right)^2$$
$$+ \frac{uvcEt^2}{3n(H_Y - H_{Y0})}\left(\arcsin\left(\frac{H_Y}{tan\alpha\sqrt{4v^2c^2 - H_Y^2}}\right) - \arcsin\left(\frac{H_Y}{tan\alpha\sqrt{4v^2c^2 - H_{Y0}^2}}\right)\right)^2$$
$$+ \frac{2uvEt(a+b)l_0}{H_Y - H_{Y0}}\left(m - \frac{mH_{Y0}}{H_Y} - ln\left(1 + m - \frac{mH_{Y0}}{H_Y}\right)\right) \tag{5}$$

Where H_{Y0} represents the initial height of YO chamber, n is the constant defining the width of the bending region over the t, and m is the constant defining the tension extent over $h_{Lu}/2$, both n and m are obtained experimentally.

As for the driving force, according to [20], the relationship between F_{YOP} and P_Y can be derived from

$$F_{YOP} = SP_Y \tag{6}$$

Where S is the effective area of YO chamber, directly related to the area of YO chamber's end face, and it can be calibrated experimentally.

To simplify the overall analysis process, further experiments and analysis about the relations of F_{PO}, H_P and P_P are conducted to analyze the mechanical properties of the PO chamber. Besides the independent analysis of the two chambers, when nested together, the height of the NDO actuator is different from the initial height of YO chamber and PO chamber, and the relationship can be derived as follows

$$H_Y = H - e_Y \tag{7}$$
$$H_P = H + (H_{P0} - H_{Y0} - e_Y) \tag{8}$$

Where H_{P0} is the initial height of PO chamber, e_Y is the height difference between YO chamber and NDO actuator in the initial state. By substituting (7) and (8) into (3), the output force of NDO actuator can be derived as follow,

$$F(H, P_Y, P_P) = F_{YOH}(H) + F_{YOP}(P_Y) + F_{POH}(H) + F_{POP}(P_P) \tag{9}$$

So far, we have explored the output force of the proposed NDO actuator, by decoupling the structure into two independent parts, and further divided the force of each part into resisting force and driving force.

5   Validation Experiments of NDO Actuator

The motion and payload capability of two independent origami chambers and the NDO actuator were experimentally tested and validated for the following reasons: (1) Their actuation characteristics were investigated to reveal the relationships between pneumatic pressure, axis displacement, and output force. (2) The coefficients to be fitted in the static-force model were quantified, and (3) The payload-enhancing effect of the proposed NDO actuator was characterized to validate the method's effectiveness. Concretely, we first present the pneumatic actuation system and experimental setup for the testing. Then, characteristic experiments for both YO chamber and PO chamber are conducted, followed by the output force experiment of NDO actuator to validate the payload improvement.

As shown in Fig. 4a, the pneumatic system is based on the Pump-value method through a controller (STM32f103c8t6, ST Inc.) to regulate two solenoid valves for each pneumatic channel. A positive pressure pump (KZP-PF, kamoer Inc.) and a vacuum pump (KVP300-KB, kamoer Inc.) work as two primary sources of pneumatic system, enabling multiple independent pneumatic supply. The airflows from the pumps pass through the air reservoirs to reduce airflow shock and ensure pressure supply. Each channel is paired with one pressure sensor (XGZP6857A, CFsensor Inc.) to produce feedback for

pressure control and to regulate the desirable pressure.

The experimental setup for testing the motion characteristics of the soft actuators was built (Fig. 4b), consisting of two linear sliding raids (HIWIN-MGN7H, 200mm.) for directional constraint, 3D-printed parts (Thermoplastic material PLA) for fixing and connecting, and a ball screw driven by step motor (6400PPR). During operation, one end of the tested actuator is fixed, and the ball screw, connected with the other end (free end) of the actuator, moves along the sliding rails to produce displacement or force interaction. At the same time, the corresponding data is recorded by pressure sensor, laser sensor (HG-C1200, Panasoinc Inc.), and 1-DOF force sensor (DYMH-103, 0-50kg, DAYSENSOR Inc.). The schematic diagram of the experimental setup is depicted in Fig. 4c.
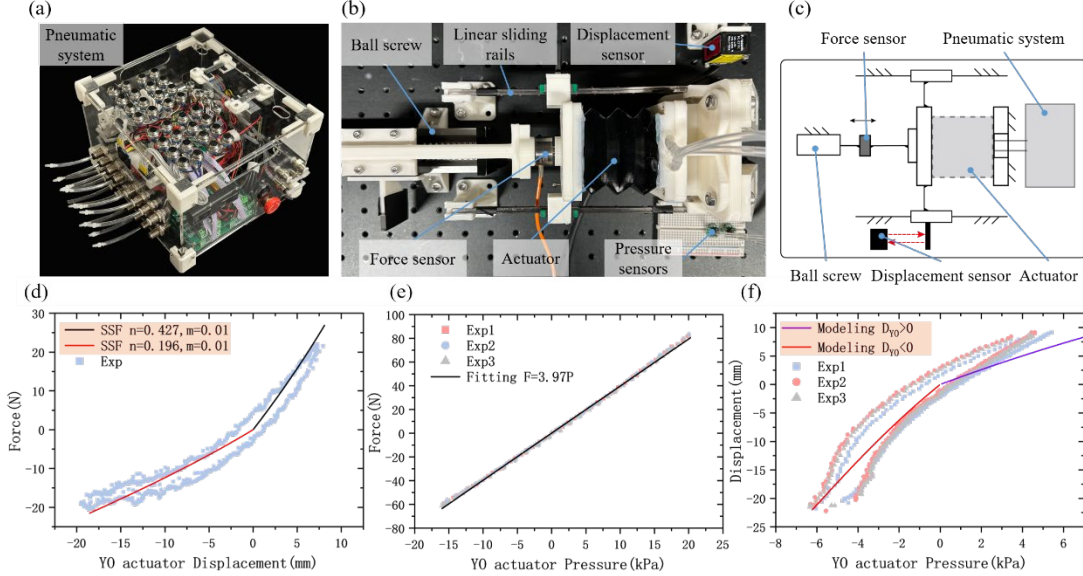

Fig. 4. Experiments to explore the statics performance of single-chamber YO chamber. (a) Pneumatic system of the experimental setup. (b) Experimental setup for exploring the relations among force, displacement and pressure of actuators. (c) Schematic representation of the setup consists of (a) and (b). (d) The bending region and tension extent of YO chamber are calibrated using the SSF principle. (e) The effective area of YO chamber is calibrated. (f) Comparison of NDO actuator in load-free state between model prediction and experimental result.

5.1 Statics Performance of YO Chamber

To explore the inherent stiffness of YO chamber, a single-chamber YO actuator was employed for the experiment. The free end of YO actuator was driven by the ball screw to move along the rails, and connected to the atmosphere. To reduce the impact of inertial motion on force measurement, the speed of the free end was designed to be relatively slow (0.4 mm/s). The data of displacement and output force was recorded. To implement the proposed model in equations (5), coefficients representing the bending region n and stretching extent m were calibrated by experiments. The data and the result predicted by the SSF principle are depicted in Fig. 4d. In the compression phase, the result came to be n=0.196, m=0.01. In the stretching phase, the result came to be n=0.427, m=0.01. By substituting the values into equations (5), a quantitative analysis of the resisting force caused by the stiffness of YO actuator can be conducted.

To explore the pressure-related driving force for YO chamber, based on the previously described configuration, the YO actuator was connected to the pneumatic system, and the free end was fixed in the initial state. The YO actuator was then pressurized and depressurized. The data of pressure and force was

recorded, as shown in Fig. 4e. The effective area S that derived in equation (6) can be obtained by calculating the slope of the fitting line, which was calculated as $S = 3.97$ N/kPa, the well-fitting of the modeling and experimental data further illustrated the control linearity of YO actuator.

The relation of the output force, height, and pressure difference of YO actuator has been derived in equation (3). With all the coefficients obtained, the state of YO actuator can now be predicted. Experiment was conducted to validate the displacement of YO actuator in a load-free state. The experimental data and the predicting result are depicted in Fig. 4f. During the testing, the ball screw and free end of YO actuator were disconnected. We then adjusted the pressure within YO actuator, and the displacement of the free end was recorded. The predicting result can well reflect the actual displacement.
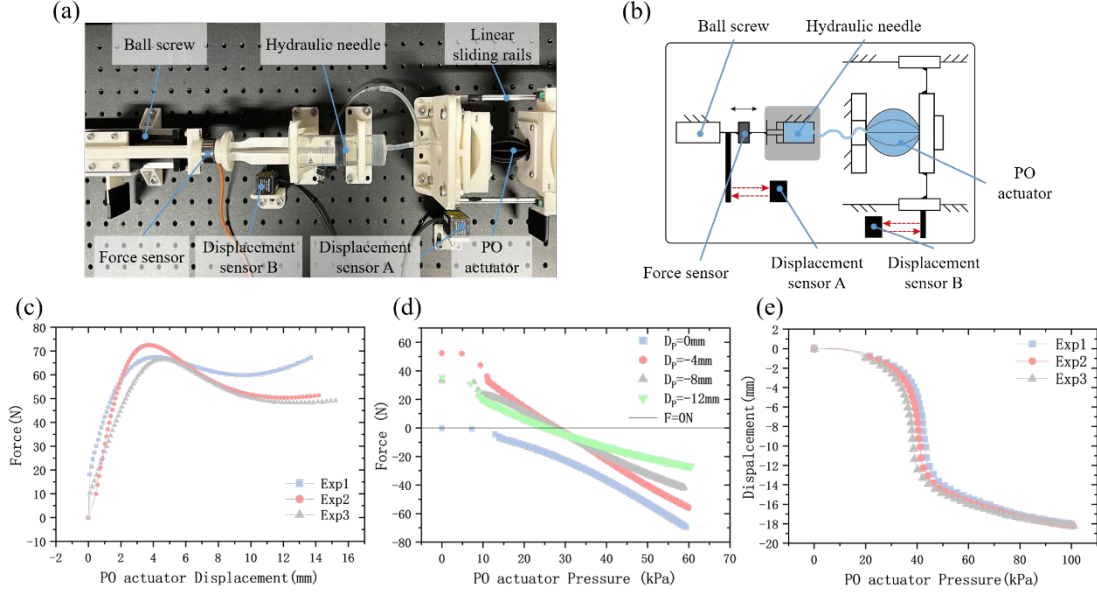

Fig. 5. Experiments to explore the statics performance of PO chamber. (a) Experimental setup for testing the stiffness of PO chamber. (b) Schematic representation of the setup. (c) Stiffness test of PO actuator. (d) Force-pressure testing of PO actuator in different displacements (D_P is the displacement of PO actuator). (e) Displacement-pressure testing of PO actuator in the load-free state.

5.2 Statics Performance of PO Chamber

To explore the resisting force (F_{POH}) of PO chamber, a single-chamber PO actuator was employed for the experiment. Another experimental setup was constructed (Fig. 5a) to obtain the resisting force during actively actuated based on the principle of virtual work, since the deformation of PO actuator when actively actuated was distinct from the passive state. The schematic diagram of the experimental setup is shown in (Fig. 5b). Building upon the mentioned setup, we interconnected a needle with the ball screw and the actuator, and the displacement of the ball screw was recorded by another displacement sensor (Displacement sensor B). The PO actuator and the additional needle were filled with nearly incompressible water. When the ball screw pushes the needle along the rails, water inside the needle flows into the PO actuator, generating a contraction movement. The displacement of PO actuator and ball screw, as well as the propulsive force, were recorded. We calculated the resisting force as follows,

$$F_{POH} \cdot dH_P = F_a \cdot dL_b \tag{10}$$

Where F_a is the propulsive force of the ball screw, dL_b is the displacement of the ball screw.

The result is depicted in Fig. 5c. The curve exhibits a similar trend to the tensile stress-strain curve of

metallic materials, indicating a linear relationship for a small segment of deformation at the initial stage of deformation.

The experiment to explore the pressure-related driving force for PO chamber followed the procedure of the same experiment for YO chamber. We tested the force-pressure relationship in 4 different displacements in order to illustrate the force enhancement effect under different compression levels (Fig. 5d). It can be learned from the result that when compressed with the displacements of -4mm, -8mm, and -12mm, the improvement in output force happened only with a pressure difference over 30kPa.

To further explore the statics of PO chamber, experiments for the relationship between displacement and pressure were conducted in the load-free state; the data is depicted in Fig. 5e. In the middle stage of the experiment, large displacement happened without an evident increasement in pressure difference, while there was only little displacement happened in the beginning and the end of the experiment.

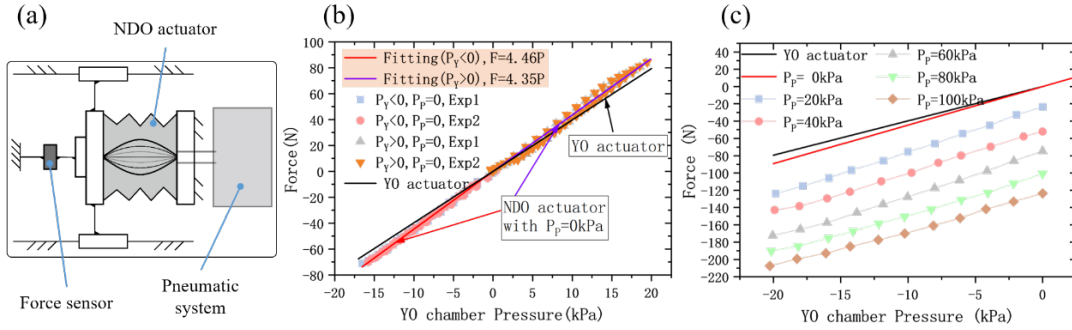### 5.3　Collaborative Payload Performance of NDO Actuator

Fig. 6. Experiments to validate the collaborative payload performance of NDO actuator. (a) Schematic representation of the setup for the payload performance of NDO actuator. (b) Force-pressure testing of NDO actuator with $P_P = 0$ kPa, comparing with the structure of single-chamber YO actuator. (c) Force-pressure testing of NDO actuator with $P_P \geq 0$ kPa.

The purpose of this work is to improve the payload performance of the existing single-chamber linear soft actuator in the direction driven by negative pressure with the newly proposed co-axial nested dual-chamber concept. Thus, after testing both the mentioned origami actuators independently, further tests were conducted in (Fig. 6a) to validate the improvement in the NDO actuator's output force capability compared with the single-chamber YO actuator in the initial state (with no displacement). The minimum pressure of YO chamber in the initial state was -20kPa, since pressure under -20kPa was likely to cause buckling on the folding facets.

The first test is to compare the YO actuator with the NDO actuator, whose PO chamber is connected to the atmosphere. The experiment data is depicted in Fig. 6a, which shows that NDO actuator inherently offered an improvement (about 10N in the contraction direction with the YO chamber's pressure of -20 kPa, increased by 12.5%; and about 8N in the elongation direction with the YO chamber's pressure of 20 kPa, increased by 10%) in payload capacity when compared with YO actuator. This is because the displacement of PO chamber is not primarily generated by the pressure difference on either side of the end caps (P_P), but rather on the pressure difference across the circumferential wall ($P_P - P_Y$). Therefore, when the YO chamber of NDO actuator is pressurized or depressurized, corresponding pressure difference arises on either side of the circumferential wall of PO chamber, and thus generates a co-directional output force, resulting in force improvement in both directions.

The second test is to validate the desirable output force improvement of NDO actuator in the direction driven by negative pressure by pressurizing the PO chamber of NDO actuator. The pressure of PO chamber was set to five evenly distributed pressure values ranging from 20 to 100 kPa, while the pressure of YO chamber was intermittently adjusted to twenty uniformly distributed pressure values ranging from 0 to -20 kPa. The output force and the corresponding pressure value are depicted in Fig. 6b, exhibiting increasing improvement in output force with increasing pressure within PO chamber. The nearly parallel lines also verified the feasibility of decoupling the two parts of output forces generated by YO chamber and PO chamber. When the PO chamber was set to 100kPa, it exhibited a great improvement in output force, which was about 130N, a nearly 162% improvement on the maximum output force of single-chamber YO actuator during the depressurizing process. These experimental results indicate that the effective payload is significantly increased in the contraction direction by the NDO structure, without diminishing the load capacity in the elongation direction, which already had a high force capacity, well proving the effectiveness of the proposed concept.

6   Conclusion and Future Work

This work presents a novel NDO structure together with CPNPA method for enhancing bidirectional payload for soft actuators, while avoiding the limited supply of single-chamber negative pressure. The NDO actuator prototype strategically combines two origami structures via coaxial nesting to significantly improve the output force of the single-chamber YO actuator in the direction driven by negative pressure without diminishing in the inverse direction. The statics models are derived analytically to endow the performance analysis and guidance of further actuation. Compared to the classical single-chamber YO structure soft actuator, on the one hand, without actively driven the inner chamber, the experimental results show that the output force can achieve a maximum of 12.5% enhancement in the contraction direction when the outer chamber is depressurized to -20kPa, and 10% enhancement in the elongation direction when the outer chamber is pressurized to 20kPa. On the other hand, based on the NDO design, with the CPNPA method, the output force in the contraction process was further increased by 130N, a nearly 162% improvement, when the inner chamber and outer chamber were applied pressure at 100 kPa and -20kPa, respectively, without diminishing the payload performance in the elongation direction at the same time. The NDO structure exhibits convenient design, easy 3D-printed fabrication and assembly for pneumatic soft actuators. Meanwhile, this structure can be convenient to assemble in various configurations for constructing soft robotic systems, broadening the application field with higher payload requirements. Future works include investigating the complete theoretical analytical force models to quantificationally analyze the influence of nested origami on actuator characteristics. Due to the NDO actuator involving a coupling dual-chamber actuation, the coupling model should also be analyzed to guide further pneumatic actuation and control. More applications should be extended to soft robots with various configurations and fields to further validate the applicability of NDO actuator. The application of similar structure for mechanical enhancement of other forms of motion like twisting and bending is also a direction of our future research.

Acknowledgments

References

1. Chen, Y.: Controlled flight of a microrobot powered by soft artificial muscles. Nature 575, 324–329 (2019).

2. Li, G.: Self-powered soft robot in the Mariana Trench. Nature 591, 66–71 (2021).

3. Xie, Z.: Octopus-inspired sensorized soft arm for environmental interaction. Science Robotics 8, eadh7852 (2023).

4. Liu, S.: Otariidae-Inspired Soft-Robotic Supernumerary Flippers by Fabric Kirigami and Origami. IEEE/ASME Transactions on Mechatronics 26, 2747–2757 (2021).

5. Fang, Z.: Omnidirectional compliance on cross-linked actuator coordination enables simultaneous multi-functions of soft modular robots. Scientific Reports 13, 12116 (2023).

6. Tang, S.: Performance enhancement of the soft robotic segment for a trunk-like arm. Frontiers in Robotics and AI 10 (2023).

7. Polygerinos, P.: Soft robotic glove for combined assistance and at-home rehabilitation. Robotics and Autonomous Systems 73, 135–143 (2015).

8. Rogatinsky, J.: A multifunctional soft robot for cardiac interventions. Science Advances 9, eadi5559 (2023).

9. Amend, J.: Soft Robotics Commercialization: Jamming Grippers from Research to Product. Soft Robotics 3, 213–222 (2016).

10. Li, S.: Fluid-driven origami-inspired artificial muscles. Proceedings of the National Academy of Sciences U.S.A. 114, 13132–13137 (2017).

11. Chen, L.: Design and modeling of a soft robotic surface with hyperelastic material. Mechanism and machine theory, 130, 109-122 (2018).

12. Xie, G.: Strong Reliable Electrostatic Actuation Based on Self-Clearing Using a Thin Conductive Layer. Soft Robotics 10, 797–807 (2023).

13. Gu, G.: Soft wall-climbing robots. Science Robotics 3, eaat2874. (2018).

14. Salerno M, Zhang K.: A novel 4-DOFs origami enabled, SMA actuated, robotic end-effector for minimally invasive surgery.2014 IEEE international conference on robotics and automation (ICRA). 2844-2849, IEEE (2014).

15. Huang, X.: Highly dynamic shape memory alloy actuator for fast moving soft robots. Advanced Materials Technologies, 4(4), 1800540 (2019).

16. Polygerinos, P.: Modeling of Soft Fiber-Reinforced Bending Actuators. IEEE Transactions on Robotics 31, 778–789 (2015).

17. Li, D. : Origami-Inspired Soft Twisting Actuator. Soft Robotics 10, 395–409 (2023).

18. Yi, J.: Customizable Three-Dimensional-Printed Origami Soft Robotic Joint With Effective Behavior Shaping for Safe Interactions. IEEE Transactions on Robotics 35, 114–123 (2019).

19. Zhang, C.: Plug & play origami modules with all-purpose deformation modes. Nature Communications 14, 4329 (2023).

20. Robertson, M.: Soft Pneumatic Actuator Fascicles for High Force and Reliability. Soft Robotics 4, 23–32 (2017).

21. Su, Y.: A High-Payload Proprioceptive Hybrid Robotic Gripper With Soft Origamic Actuators. IEEE Robotics and Automation Letters 5, 3003–3010 (2020).

22. Yi, J.: Fiber-Reinforced Origamic Robotic Actuator. Soft Robotics 5, 81–92 (2018).

23. Zhang, Z.: Bioinspired Rigid-Soft Hybrid Origami Actuator With Controllable Versatile Motion and Variable Stiffness. IEEE Transactions on Robotics 39, 4768–4784 (2023).

24. Zhu, R.: Soft robots for cluttered environments based on origami anisotropic stiffness structure (OASS) inspired by desert Iguana. Advanced Intelligent Systems, 5(6), 2200301 (2023).

25. Dong, X.: Increasing the Payload and Terrain Adaptivity of an Untethered Crawling Robot Via Soft-Rigid Coupled Linear Actuators. IEEE Robotics and Automation Letters 6, 2405–2412 (2021).

26. Lee, J.-G.: Origami-Based Vacuum Pneumatic Artificial Muscles with Large Contraction Ratios. Soft Robotics 6, 109–117 (2019).

27. Paez, L.: Design and Analysis of a Soft Pneumatic Actuator with Origami Shell Reinforcement. Soft Robotics 3, 109–119 (2016).

28. Feng, M.: X-crossing pneumatic artificial muscles. Science Advances 9, eadi7133 (2023).

29. Liu, S.: Small-strain folding of semi-rigid elastomer derives high-performance 3D-printable soft origami actuators. Chemical Engineering Journal 489, 151462 (2024).

30. De Pascali C.:3D-printed biomimetic artificial muscles using soft actuators that contract and elongate. Science Robotics 7: eabn4155. (2022).